

Low-temperature ammonia synthesis on electron-rich $[RuH_6]$ catalytic centers

Received 00th January 20xx,
Accepted 00th January 20xx

Jaysree Pan^{1†}, Qianru Wang^{2,3†}, Jianping Guo^{2,3}, Heine Anton Hansen¹, Ping Chen^{2,3,4*}, Tejs Vegge^{1*}

DOI: 10.1039/x0xx00000x

Ammonia is a central vector in sustainable global growth, but the usage of fossil feedstocks and centralized Haber-Bosch synthesis conditions causes >1.4% of the global anthropogenic CO_2 emissions. While nitrogenase enzymes convert atmospheric N_2 to ammonia at ambient conditions, even the most active manmade inorganic catalysts fail due to low activity and parasitic hydrogen evolution at low temperatures. Here, we show the $[RuH_6]$ catalytic center in ternary ruthenium complex hydrides (Li_4RuH_6 and Ba_2RuH_6) activate N_2 preferentially and avoid hydrogen over-saturation at low temperatures and near ambient pressure by delicately balancing H_2 chemisorption and N_2 activation. The active $[RuH_6]$ catalytic center is capable of achieving an unprecedented yield at low temperatures via a shift in the rate-determining reaction intermediates and transition states, where the reaction orders in hydrogen and ammonia change dramatically. Temperature-dependent atomic-scale understanding of this unique mechanism is obtained with synchronized experimental and density functional theory investigations.

Introduction

Ammonia is critical to our food production ecosystem^{1,2} and the single most produced polluting chemical (~170 million tons per year)^{3–5}, while also holding the potential to become one of the most promising carbon-free and low-cost long term energy carrier^{6,7}. The industrial Haber-Bosch (H-B) process employs a Fe-based catalyst, fossil-fuel sourced H_2 , and requires harsh operating conditions (typically 673–723 K and 100–300 bar of pressure). The large-scale and centralized H-B process accounts for nearly 2% of the world's consumption of fossil fuels⁸, and consequently over 1.44% of the global anthropogenic CO_2 emissions⁵. The development of small-scale processes that rely on renewable electricity as an energy source to sustainably produce the H_2 feedstock would thus be transformative in several ways. It would provide critical technological support towards the audacious goal of carbon-free growth and ensuring the green transition. Two indispensable targets would be reached simultaneously, where renewable energy penetration is arduous – food production and clean mobility^{4,9}. A decentralized, low CAPEX NH_3 synthesis process targeted at emerging markets with significant future population growth needs would also support the core U.N. sustainability goals.

While direct electrochemical ammonia production represents the Holy Grail, the documented yields remain very far from any kind of commercialization¹⁰. The discovery of efficient heterogeneous or homogeneous catalysts that exhibit high activity under mild

conditions would thus be a key enabler for the decentralized production of green ammonia. For industrial ammonia synthesis, it is widely recognized that Ru-based catalysts work better than Fe-based catalysts under milder reaction conditions^{11,12}. However, the high activation energy for direct N_2 dissociation and the severe poisoning effect of hydrogen on conventional Ru metal catalyst renders efficient NH_3 synthesis under lower temperatures (< 623 K) and lower pressures (< 50 bar) unattainable¹³. Therefore, many attempts to develop new catalysts for efficiently catalyzing N_2+H_2 to NH_3 under mild conditions^{14–17}. Recently discovered, a new class of ammonia catalysts – the ternary ruthenium complex hydrides¹⁸ is a breakthrough in this endeavor. The ternary ruthenium hydride's ability to efficiently synthesize NH_3 at <10 bar and < 573 K conditions lies in the unique chemistry of the coordination complex and the alkali (alkaline earth) metal framework, facilitating a catalytic mechanism bridging homogeneous and heterogeneous concepts, which are clearly distinct from the Ru metal catalyst. For ternary Ru complex hydride catalysts, Ru is in an ionic state, and N_2 undergoes non-dissociative hydrogenolysis over the hydride(H^-)-rich and electron-rich $[RuH_6]^{4-}$ complex with the aid of the surrounding Li or Ba cations. The dynamic and synergistic engagement of all the components of the ternary hydrides creates a reaction path with a narrow energy span and leads to ammonia production with superior activities.

In this paper, we present the reaction mechanism facilitating ternary ruthenium complex hydrides to successfully produce NH_3 at low temperature ($448\text{ K} \leq T \leq 573\text{ K}$) by selective N_2 activation and escaping H_2 over-saturation. This work shows the unique ability of the $[RuH_6]^{4-}$ catalytic center in the ternary ruthenium hydride to shift its rate-determining intermediate states and transition states of the N_2+H_2 to NH_3 reaction path in response to the lowering of the reaction temperature, which brings a significant change in reaction order of hydrogen and ammonia. This variation in the kinetics as a function of operating conditions (temperature, reactant partial pressures, etc.) is not a common phenomenon in catalysis but is observed in some cases^{19–23}. Nonetheless, the mechanistic details

¹ Department of Energy Conversion and Storage, Technical University of Denmark, 2800 Kgs. Lyngby, Denmark.

² Dalian National Laboratory for Clean Energy, Dalian Institute of Chemical Physics, Chinese Academy of Sciences, Dalian, China.

³ University of Chinese Academy of Sciences, Beijing, China.

⁴ State Key Laboratory of Catalysis, Dalian, China.

*Correspondence to: Tejs Vegge (teve@dtu.dk); Ping Chen (pchen@dicp.ac.cn)

† These authors contributed equally to this work.

Electronic Supplementary Information (ESI) available: [details of any supplementary information available should be included here]. See DOI: 10.1039/x0xx00000x

behind it are seldom investigated, especially at an atomic level. Here, we achieve this via seamless integration of experimental and computational techniques to reveal the temperature-dependent catalytic process. Our finding discloses that an electron-rich active center with a comparable affinity towards N_2 and H_2 are critical for mild-condition ammonia catalysis. The thorough fundamental understanding developed in this study can be further used to design new low-temperature ammonia catalysts with better performance and has the potential to drive the green ammonia technology into a new direction.

Results and discussion

Figure 1 shows that the $[RuH_6]$ catalytic center in Ru complex hydride catalysts (Li_4RuH_6 and Ba_2RuH_6) not only outperforms the $B5$ site of Ru metal catalysts under the same working conditions but also produces NH_3 at low temperatures. As discussed below, two inherent properties of the $[RuH_6]$ catalytic center are critical towards the observed outstanding activity at low temperatures: (a) its selectivity for chemisorbing N_2 over H_2 and (b) a self-adjusting mechanism of avoiding hydrogen over-saturation sustaining the N_2 to NH_3 conversion cycle.

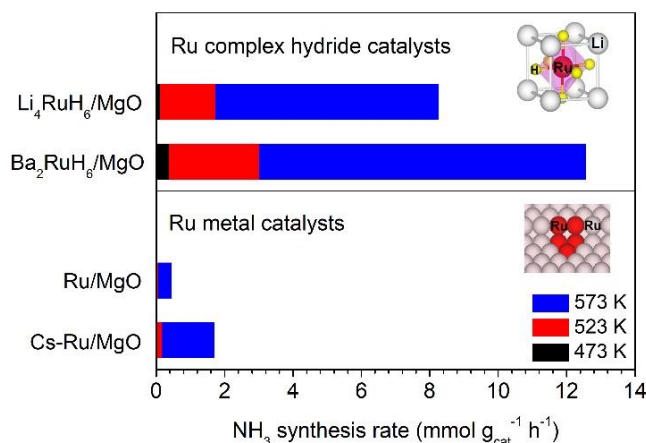


Figure 1 Comparison of NH_3 synthesis rate and active site structure of ternary Ru complex hydride catalysts and Ru metal catalysts. Reaction conditions: 1 bar of syngas, $N_2:H_2=1:3$, and a weight hourly space velocity (WHSV) of 60000 ml $g^{-1} h^{-1}$.

The catalytically active ternary hydride surface with excess Li and hydrogen (consists of two additional LiH for every six $[RuH_6]$ centers, i.e., $4[RuH_6]+2[RuH_7]+2Li$)¹⁸ is energetically moderately selective towards N_2 over H_2 chemisorption. The model considered (110) plane of Li_4RuH_6 , which is the most stable crystal face for this material (Figure 2A). The details of the Li_4RuH_6 active surface used for this study are in Figures 2B and 2C. The presence of additional two Li and two H (from two LiH) on the surface breaks its local symmetry. As a result, one of the $[RuH_6]$ polyhedral turns into a pentagonal based pyramidal instead of standard octahedral. This $[RuH_6]$ site (denoted as $[RuH_6]^*$) with pentagonal based pyramidal polyhedral is the preferred site for N_2/H_2 adsorption compared to other $[RuH_6]$ sites

with the octahedral coordination due to lower steric hindrance (Figure S1). In contrast, $[RuH_7]$ sites on the Li_4RuH_6 active surface can not adsorb further any N_2/H_2 . The extra two Li (from additional LiH) on the surface also create hindrances for N_2/H_2 adsorption on other neighbouring $[RuH_6]$ sites and cause partial deactivation. However, other $[RuH_6]/[RuH_7]$ sites and extra Li on the surface are vital for the N_2+H_2 to NH_3 conversion process¹⁸. The $[RuH_7]/[RuH_6]$ on the Li_4RuH_6 active surface act as a reservoir of hydrides to reduce the activated N_2 to NH_3 . The electrostatic interaction between surface Li and intermediate N_xH_y ($x=1-2$, $y=0-4$) species lowers the reaction path's thermodynamic/kinetic barrier, thus facilitating the N_2+H_2 to NH_3 catalysis.

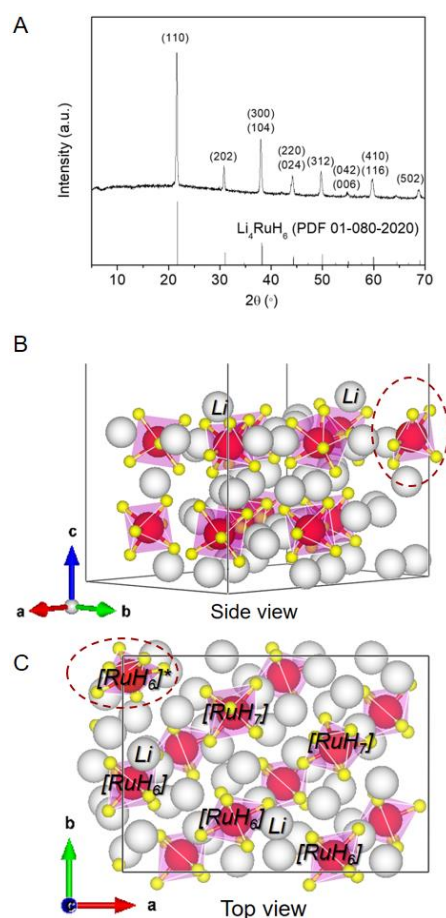


Figure 2 A The XRD pattern of the as-prepared Li_4RuH_6 sample demonstrating (110) plane as its most stable façade. The Miller indexes are marked above the corresponding peaks. B and C are respectively the side, and top view of the catalytic active ternary hydride surface, i.e., Li_4RuH_6 surface with two extra LiH dissociatively adsorbed on it. Plot B shows the four-layered Li_4RuH_6 slab's side view with two Li ions from the additional two LiH on the surface. Plot C is the top view of the surface, highlighting four $[RuH_6]$ and two $[RuH_7]$ (accommodating two H s from the two LiH) complexes. The dissociative addition of two LiH on the surface breaks the surface symmetry locally, and one of the $[RuH_6]$ complex transformed into a pentagonal based pyramidal polyhedral (marked by the circular enclosure) from an octahedral polyhedral. Color code: Li -light gray, Ru -red, and H -yellow.

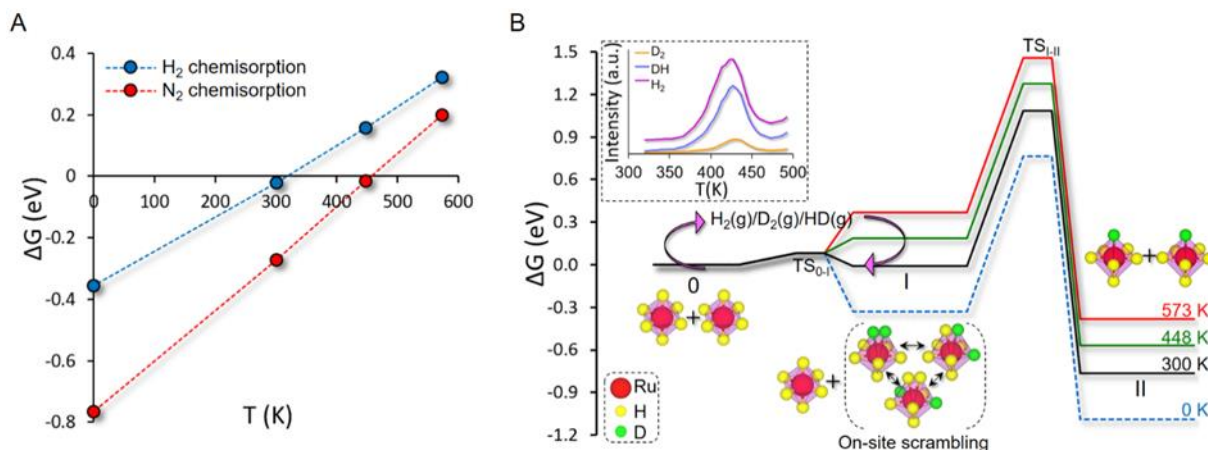
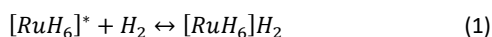
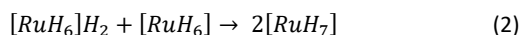


Figure 3 **A** The competitive chemisorption of N_2 and H_2 by the $[RuH_6]$ center on the Li_4RuH_6 catalyst surface shows selectivity for N_2 over H_2 , which improves at lower temperature and, **B** the free energy path of H_2/D_2 chemisorption/desorption along with on-site scrambling of the chemisorbed H_2/D_2 on the Li_4RuH_6 catalyst surface and a prohibitively high barrier (> 1 eV) for chemisorbed H_2 to lattice H transfer demonstrates the mechanism by which $[RuH_6]$ catalytic center avoids hydrogen over-saturation. The top insertion in **B**, shows the TPD profile of deuterated Li_4RuH_6 .

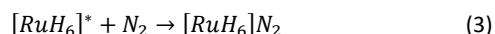
The chemisorption H_2 on the Li_4RuH_6 active surface here can be expressed as:



For simplicity, we are representing the Li_4RuH_6 active surface (which has four $[RuH_6]$ complex, two $[RuH_7]$ complex, and two extra Li) only by the active catalytic site $[RuH_6]^*$. Here, the lattice hydrogens of Ru are inside the square brackets ($[RuH_6]/[RuH_7]$). The chemisorbed H_2 remains molecular ($[RuH_6]H_2$) till the $H-H$ bond breaks (one of the hydrogens goes to the neighboring Ru ($[RuH_6]$)) and becomes part of the lattice and creates two $[RuH_7]$ in the process (see Figure S2). The transformation of the chemisorbed H_2 to lattice H can be written as:



Meanwhile, the competitive chemisorption of N_2 on the Li_4RuH_6 active surface is:



The calculated binding free energies show that the preferential adsorption of N_2 over H_2 at the $[RuH_6]^*$ active center is further enhanced at lower temperatures (Figure 3A). This feature is critical for the understanding of the catalytic mechanism, particularly when combined with the kinetics of dissociative hydrogen chemisorption and hydrogen transfer over the $[RuH_6]$ centers. Figure 3B displays the free energy landscape for dissociation of chemisorbed H_2 (state-I) on the $[RuH_6]$ active center (eqn.(2)). Although the dissociative chemisorption of H_2 into two lattice H s is facile, the subsequent transfer of lattice H , as $[RuH_7]$ (state-II), via a transition state (TS_{I-II}), is prohibited by a high activation energy of 1.1 eV (Figure S2) as estimated with nudged elastic band simulations. The transfer of the chemisorbed H_2 to lattice H is Li -mediated and encounters repulsive force from neighboring H s, making the activation barrier high. Instead, at low temperature, the active center retains the hydrogen atoms to form a $[RuH_6]H_2$ complex (state-I), which is not a very stable state and can easily desorb H_2 at temperatures above 300 K to release the $[RuH_6]$ catalytic site for N_2 activation (see Figure 3B). The mechanism of H_2 chemisorption/desorption ensures not all $[RuH_6]$ centers are converted to $[RuH_7]$ complexes, even in an H_2 -rich environment. Thus, the catalyst surface is not hydrogen over-

saturated by lattice H that bonds firmly to the respective Ru blocking the active sites. This contrasts with Ru and other late transition metal catalysts, where H -poisoning, due to favorable thermodynamics²⁴ effectively prevents N_2 adsorption. The opposing behavior between Ru metal and Li_4RuH_6 catalysts is elegantly captured in the NH_3 formation rate under varying pressure (Figure S3). The lack of hydrogen poisoning effect allows enhanced ammonia production at a higher hydrogen partial pressure on Li_4RuH_6 .

The chemisorption of H_2 on the ternary hydride active surface has unique fingerprints (Figure 3B). The chemisorption of H_2 happens through a physisorbed transition state TS_{0-I} , with a negligible barrier of 0.07 eV (Figure S4). The H from the chemisorbed H_2 participates in on-site scrambling with the lattice H on the $[RuH_6]$ active center. The on-site scrambling of the hydrogen has an insignificant activation energy of 0.04 eV (Figure S5). Experimentally, we observe a minor reversible adsorption/desorption of H_2 in the temperature range of 373 K to 473 K in the temperature programmed desorption (TPD) profile with no trace of net LiH , Ru powder, or a mixture of LiH and Ru (Figure S6), which reinforces the observation of the chemisorbed nature of the H_2 adsorption on the Li_4RuH_6 active surface. After charging with D_2 , the detection of the mixed HD signal in the TPD profile strengthens the conclusion of the on-site scrambling of D from chemisorbed D_2 with lattice H (inserted plot of Figure 3B). A more robust signal of H_2/HD than D_2 in the TPD profile points out the magnitude of the on-site scrambling of the chemisorbed D_2 with the lattice H .

Our study shows that the N_2+H_2 to NH_3 conversion cycle on the Li_4RuH_6 catalyst surface happens through 13 different surface states (states 0-12). Visualization of the NH_3 formation mechanism on the Li_4RuH_6 catalyst surface with intermediate states is provided in Figure 4.

Here, the state-0 and state-1 are the Li_4RuH_6 catalyst surface with active $[RuH_6]$ center and the chemisorbed N_2 on it ($[RuH_6]NN$), respectively, as presented by the eqn.(3). The state-2 is ($[RuH_5]NHN$), where the adsorbed N_2 is hydrogenated by one of the hydrides from the same Ru site where N_2 is activated (i.e., H from $[RuH_6]-NN$):



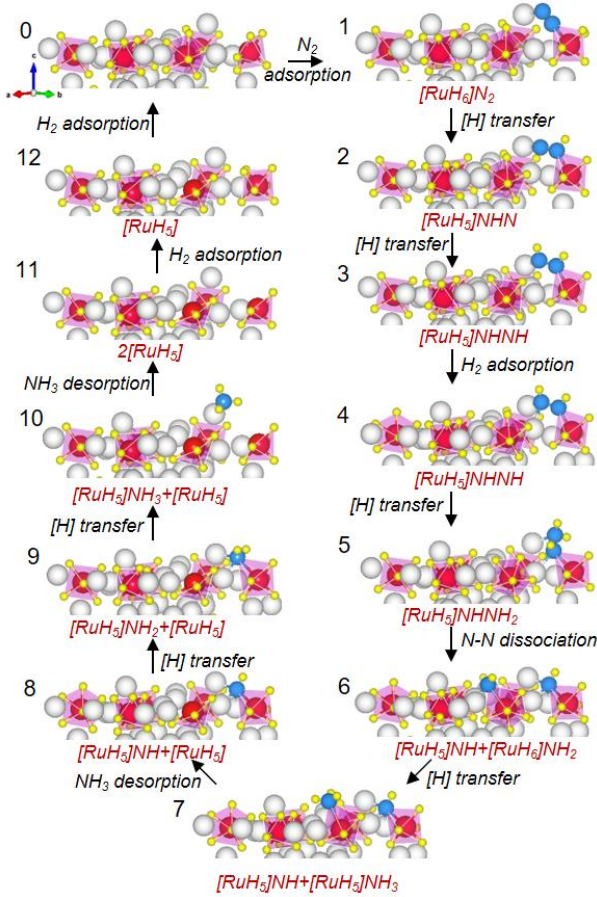
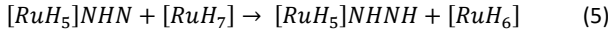
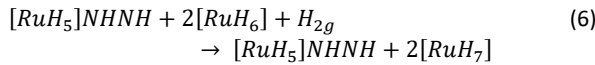


Figure 4 Visualization of the N_2 to NH_3 conversion path on the Li_4RuH_6 catalyst surface. The catalytic conversion cycle went through 13 different surface states (marked by 0-12). The hydrogenation of the activated nitrogen by the lattice hydrogen is marked as "[H] transfer". Color code: Li-light gray, Ru-red, H-yellow, and N-blue.

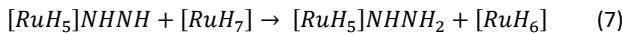
State-3 is ($[RuH_5]NHNH$), in which the activated N_2 is further hydrogenated by one hydride from neighboring $[RuH_7]$:



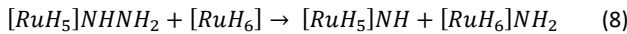
In state-4 ($[RuH_5]NHNH_2 + 2[RuH_7]$), one $H_2(g)$ gaseous molecule chemisorbs and then dissociates into two lattice hydrogens on the surface:



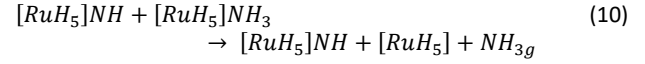
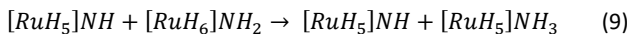
State-5 is ($[RuH_5]NHNH_2$), where the activated N_2 is further hydrogenated from one hydride of an adjacent $[RuH_7]$ site:



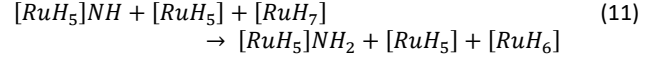
In state-6 ($[RuH_5]NH + [RuH_6]NH_2$), the N-N bond fully dissociates:



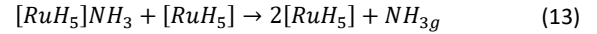
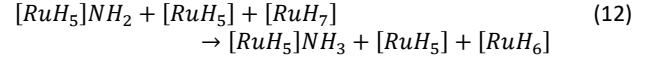
In state-7 ($[RuH_5]NH + [RuH_5]NH_3$), the first molecule of NH_3 is formed, which then desorbs from the surface and creates state-8 ($[RuH_5]NH + [RuH_5]$):



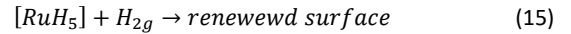
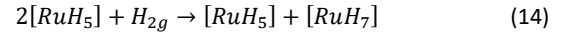
In state-9 ($[RuH_5]NH_2 + [RuH_5]$), the remaining N is hydrogenated further from the hydrides of an adjacent $[RuH_7]$ site:



The 2nd molecule of NH_3 is formed in state-10 ($[RuH_5]NH_3 + [RuH_5]$), which then desorbs from the surface and results in state-11 ($2[RuH_5]$):



Two consecutive direct adsorptions of $H_2(g)$ molecule replenish the two hydride-deficient $[RuH_5]$ sites on the state-11, result in state-12 ($[RuH_5]$) and then finally back to state-0:



The overall chemical reaction in one catalytic cycle on Li_4RuH_6 catalyst surface is:



The path shows a series of well-balanced and moderate activation energies – all with $E_a \leq 0.82$ eV (see Table S1).

For better understanding the low temperature reaction pathway, the variations of reaction energetics as a function of temperature are explored and then analyzed by applying the energetic span model, in which the turnover frequency (TOF) determining transition state ($TDTS$) and TOF determining intermediate state (TDI) that maximize the energy span determine the rates and kinetics of the catalytic cycle^{24,25}. The energetic span approximation²⁵ of the exothermal catalytic cycle to calculate turn over frequency (TOF) from the energetic span (δE) of the free energy path:

$$TOF = \frac{k_B T}{h} e^{-\delta E / k_B T} \quad (17)$$

In this model, the free energy of TOF -determining transition state (ΔG_{TDTS}), TOF -determining intermediate state (ΔG_{TDI}) and the free energy of reaction (ΔG_r) defines δE :

$$\delta E = \begin{cases} \Delta G_{TDTS} - \Delta G_{TDI}, & \text{if } TDTS \text{ appears after } TDI \\ \Delta G_{TDTS} - \Delta G_{TDI} + \Delta G_r, & \text{if } TDTS \text{ appears before } TDI \end{cases} \quad (18)$$

The activation enthalpy (ΔH_a) for the catalytic path is back-calculated from the δE and the entropy correction ($T\Delta S$):

$$\Delta H_a = \delta E + T\Delta S \quad (19)$$

Figure 5 (and Figure S7) shows the development of the free energy path of the catalytic cycle of $N_2 + H_2$ to NH_3 on the Li_4RuH_6 catalyst surface with a lowering of reaction temperature ($448 \text{ K} \leq T \leq 573 \text{ K}$).

The change in temperature shifts the *TDI* and *TDTS* of the catalytic cycle, with an inflection temperature being at 498 K. Experimentally, the Arrhenius plot for ammonia synthesis (Figure 6A) locates this inflection point around 523 K. In addition, all measured kinetic

parameters for ternary hydride catalyst ($\text{Li}_4\text{RuH}_6/\text{MgO}$) are temperature-dependent (Figure 6), indicating the complex temperature-dependent switching of rate-determining states (i.e. *TDI* and *TDTS*).

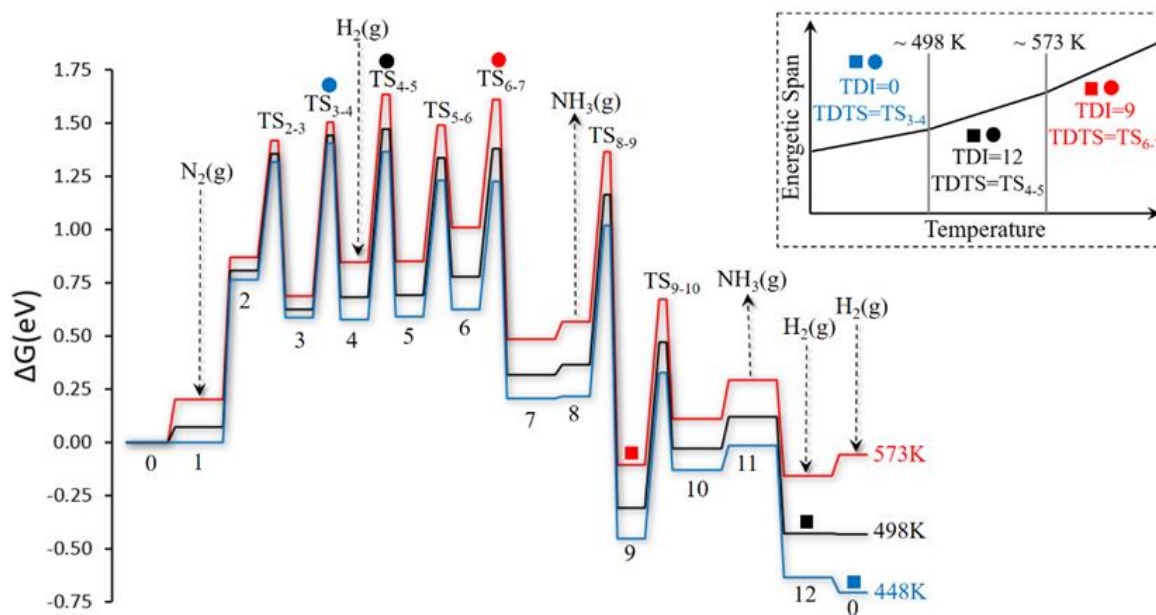


Figure 5 The evolution of the free energy path with the lowering of temperature shifts the *TDI* and the *TDTS* of the energetic span model, and the inflection point is at 498 K of Li_4RuH_6 catalyst surface. For the lower temperature range (< 498 K), the *TDI* and *TDTS* are the initial/final state (state-0) and the transition state of the third hydrogenation (TS_{3-4}) on the surface, respectively. In the higher temperature range (≥ 498 K), the *TDI* and the *TDTS* are the second $\text{H}_2(\text{g})$ adsorption (state-12) and the transition state of the first $\text{H}_2(\text{g})$ adsorption (TS_{4-5}) on the surface respectively. With further increase in temperature, state-9 comes energetically closer to state-12. At 573 K, the *TDI* and the *TDTS* are state-9 and TS_{4-5} , respectively. The inserted plot shows the schematic presentation of the shift in *TDI*/*TDTS*. The *TDI* and *TDTS* at different temperature ranges are marked by the square- and circle-symbols, respectively, in the free energy plot and the inserted plot. We applied a fixed total pressure of 1 bar ($\text{N}_2:\text{H}_2=1:3$) to generate the free energy paths and barriers using density functional theory based free energy estimations and nudged elastic band method.

As shown in Figure 5, the *TDTS* moves from the transition state 4-5 (TS_{4-5}) to TS_{3-4} as the temperature goes lower than the inflection point 498 K. Meanwhile, the *TDI* shifts from state 12 to state 0. For clarity, the inserted plot in Figure 5 presents a schematic view of the shift in *TDI*/*TDTS* with temperature. There might be one inflection for each change in *TDI*/*TDTS*, which we can not resolve due to their proximity. Another essential feature in the catalytic path is the energy difference between state 12 and state 9. At 573 K, the free energies of states 9 and 12 are similar, and they are both likely candidates for the *TDI*. The energy difference between state 12 and state 9 increases with decreasing temperature, and the state 12 is *TDI* in the range $498 \text{ K} < T < 573 \text{ K}$. The theoretically derived activation

enthalpy (ΔH_a) and *TOF*, and experimentally derived apparent activation energy (E_{app}) and *TOF* are listed in Table S2. The value of ΔH_a at 448 K is 98.2 kJ mol^{-1} . While at 573 K, with state 9 as *TDI*, the ΔH_a is calculated to be 72.4 kJ mol^{-1} . An increase in temperature lowers the activation enthalpy and increases the *TOF*, agreeing well with the trends observed experimentally. The apparent activation energy for Li_4RuH_6 catalyst determined by Arrhenius plot is $E_{app} = 71.2 \text{ kJ/mol}$ at temperatures higher than 523 K, and significantly increased value of 102.8 kJ/mol at temperatures below 523 K (Figure 6A). In contrast, there is no change in E_{app} and other kinetic parameters for conventional Ru metal catalyst (Ru/MgO) in a wide temperature range (498-648 K).

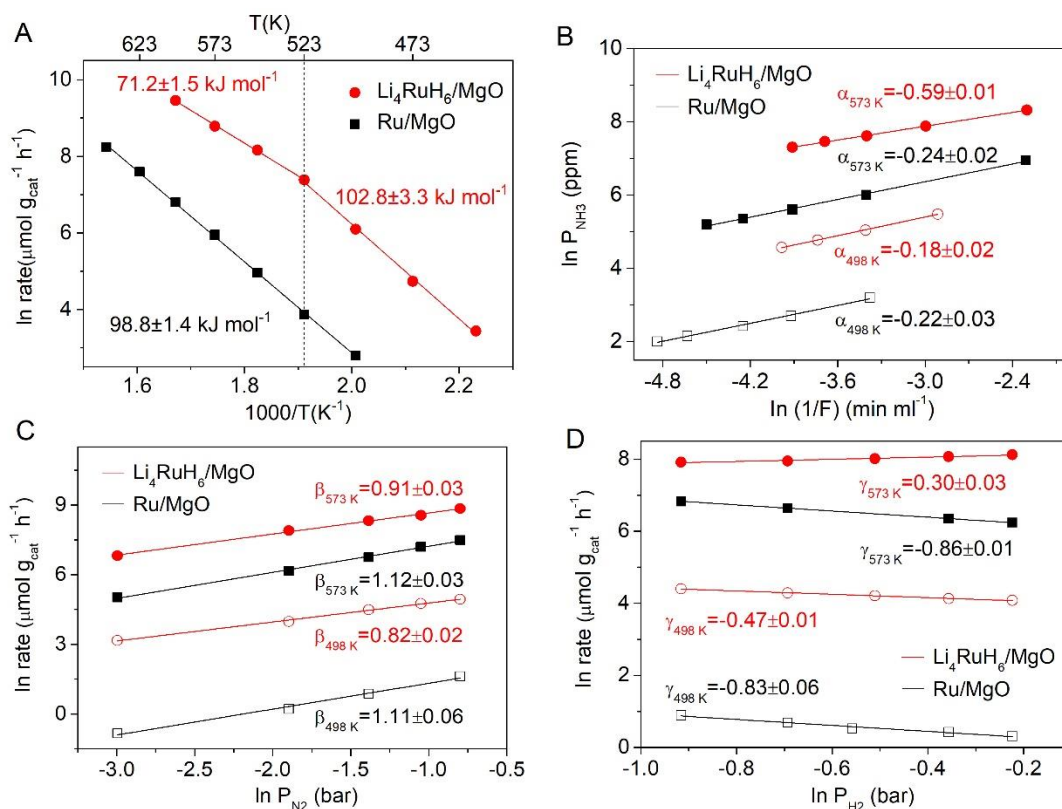


Figure 6 Experimentally derived kinetic parameters. **A** Arrhenius plots of supported $\text{Li}_4\text{RuH}_6/\text{MgO}$ and Ru/MgO catalysts. **B** to **D** dependence of ammonia synthesis rates on the partial pressures of NH_3 , N_2 , and H_2 , respectively, under a total pressure of 1 bar at 573 K (filled symbols) and 498 K (open symbols) over supported $\text{Li}_4\text{RuH}_6/\text{MgO}$ and Ru/MgO catalysts. The reaction order of NH_3 , N_2 , and H_2 is represented by α , β , and γ , respectively.

For Li_4RuH_6 catalyst, the energetic span and the TOF vary continuously with temperature. The temperature dependent TDI and TDTS modifications follow the entropy of intermediates and transition states. The entropy of a state is strongly affected by the adsorption/desorption of gas molecules. Such changes in the TDI or TDTS will tend to affect both ΔH_0 and the reaction order in gas molecules. This is beautifully captured by the analysis of the reaction order of NH_3 , N_2 , and H_2 for Li_4RuH_6 (Figure 6B-D). The reaction orders changed from +0.3 to -0.47, 0.91 to 0.82, and -0.59 to -0.18 respectively for H_2 , N_2 , and NH_3 with the decrease of temperature. These changes are in stark contrast to the constant values for Ru metal catalyst (Ru/MgO), i.e., -0.23, 1.12, and -0.85, respectively for H_2 , N_2 , and NH_3 . It is worth noting that, although the H_2 reaction orders of ternary Ru hydride catalysts decrease with the decrease of temperature, they are still higher than that of the Ru metal catalyst. Moreover, NH_3 poisoning effects on the $[\text{RuH}_6]$ center lessens at lower temperatures, providing a favorable scenario for effective catalysis.

Conclusions

The present study highlights the dynamic nature of the $[\text{RuH}_6]$ catalytic center in enabling mild condition ammonia synthesis. The presence of $[\text{RuH}_7]$ complex facilitates the hydrogenation of the activated nitrogen from the surplus lattice hydrides. On the contrary, a too high concentration of $[\text{RuH}_7]$ complex on the surface can deactivate the catalyst from dinitrogen adsorption. The high activation energy for lattice H transfer of the chemisorbed H_2 observed in this unique class of material maintains a delicate balance between the availability of lattice hydrogen and active sites. The

preferential N_2 chemisorption over H_2 and kinetic blockage of hydrogen over-saturation are key elements to the success of ternary Ru complex hydride systems for catalyzing NH_3 synthesis at low temperatures. Furthermore, a unique temperature-dependent tuning of the reaction kinetics is observed for $[\text{RuH}_6]$ catalytic center, resulting from a shift in the TDI and TDTS along the reaction pathway.

We have been able to achieve a precise temperature resolved atomic-scale understanding of the reaction mechanism at the $[\text{RuH}_6]$ catalytic center, its unique thermodynamics, and kinetic aspects that enable exceptional low-temperature activity. These scientific insights need to be exploited towards optimizing complex transition metal hydrides as ammonia catalysts as well as exploring a newer class of materials that can replicate the behavior of $[\text{RuH}_6]$ catalytic center in the pursuit of renewables powered decentralized room temperature/pressure ammonia synthesis.

Conflicts of interest

The authors declare no competing financial interest

Acknowledgments

J.P, H.H and T.V. thank the Velux Foundations for financial support through the research center V-Sustain (#9455). TV also acknowledges support from the Independent Research Fund

Denmark (DELIGHT#0217-00326B). Q.W, P.C. and J.G. thank the financial support from National Natural Science Foundation of China (Grant Nos. 21633011, 21922205 and 21988101), Dalian Institute of Chemical Physics (DCLS201702), and K. C. Wong Education Foundation (GJTD-2018-06).

- 24 S. Kozuch, *WIREs Computational Molecular Science*, 2012, **2**, 795–815.
25 S. Kozuch and S. Shaik, *Acc. Chem. Res.*, 2011, **44**, 101–110.

Notes and references

- 1 V. Smil, *Nature*, 1999, **400**, 415–415.
- 2 J. W. Erisman, M. A. Sutton, J. Galloway, Z. Klimont and W. Winiwarter, *Nature Geoscience*, 2008, **1**, 636–639.
- 3 Periodic Graphics, <https://cen.acs.org/energy/Periodic-Graphics-Environmental-impact-industrial/97/i24>, (accessed June 30, 2020).
- 4 P. H. Pfromm, *Journal of Renewable and Sustainable Energy*, 2017, **9**, 034702.
- 5 G. Soloveichik, *Nature Catalysis*, 2019, **2**, 377–380.
- 6 A. Valera-Medina, H. Xiao, M. Owen-Jones, W. I. F. David and P. J. Bowen, *Progress in Energy and Combustion Science*, 2018, **69**, 63–102.
- 7 A. Klerke, C. H. Christensen, J. K. Nørskov and T. Vegge, *J. Mater. Chem.*, 2008, **18**, 2304–2310.
- 8 Q. Wang, J. Guo and P. Chen, *Journal of Energy Chemistry*, 2019, **36**, 25–36.
- 9 S. Giddey, S. P. S. Badwal, C. Munnings and M. Dolan, *ACS Sustainable Chem. Eng.*, 2017, **5**, 10231–10239.
- 10 S. Z. Andersen, V. Čolić, S. Yang, J. A. Schwalbe, A. C. Nielander, J. M. McEnaney, K. Enemark-Rasmussen, J. G. Baker, A. R. Singh, B. A. Rohr, M. J. Statt, S. J. Blair, S. Mezzavilla, J. Kibsgaard, P. C. K. Vesborg, M. Cargnello, S. F. Bent, T. F. Jaramillo, I. E. L. Stephens, J. K. Nørskov and I. Chorkendorff, *Nature*, 2019, **570**, 504–508.
- 11 K. Aika, *Catalysis Today*, 2017, **286**, 14–20.
- 12 D. E. Brown, T. Edmonds, R. W. Joyner, J. J. McCarroll and S. R. Tennison, *Catal Lett*, 2014, **144**, 545–552.
- 13 A. Vojvodic, A. J. Medford, F. Studt, F. Abild-Pedersen, T. S. Khan, T. Bligaard and J. K. Nørskov, *Chemical Physics Letters*, 2014, **598**, 108–112.
- 14 P. Wang, F. Chang, W. Gao, J. Guo, G. Wu, T. He and P. Chen, *Nature Chemistry*, 2017, **9**, 64–70.
- 15 M. Kitano, Y. Inoue, Y. Yamazaki, F. Hayashi, S. Kanbara, S. Matsuishi, T. Yokoyama, S.-W. Kim, M. Hara and H. Hosono, *Nature Chemistry*, 2012, **4**, 934–940.
- 16 Y. Gong, J. Wu, M. Kitano, J. Wang, T.-N. Ye, J. Li, Y. Kobayashi, K. Kishida, H. Abe, Y. Niwa, H. Yang, T. Tada and H. Hosono, *Nature Catalysis*, 2018, **1**, 178–185.
- 17 S. L. Foster, S. I. P. Bakovic, R. D. Duda, S. Maheshwari, R. D. Milton, S. D. Minter, M. J. Janik, J. N. Renner and L. F. Greenlee, *Nature Catalysis*, 2018, **1**, 490–500.
- 18 Q. Wang, J. Pan, J. Guo, H. A. Hansen, H. Xie, L. Jiang, L. Hua, H. Li, Y. Guan, P. Wang, W. Gao, L. Liu, H. Cao, Z. Xiong, T. Vegge and P. Chen, , DOI:10.26434/chemrxiv.13465760.v1.
- 19 Y.-G. Wang, D. C. Cantu, M.-S. Lee, J. Li, V.-A. Glezakou and R. Rousseau, *J. Am. Chem. Soc.*, 2016, **138**, 10467–10476.
- 20 J. Xu, Y.-Q. Deng, X.-M. Zhang, Y. Luo, W. Mao, X.-J. Yang, L. Ouyang, P. Tian and Y.-F. Han, *ACS Catal.*, 2014, **4**, 4106–4115.
- 21 T. Fujita, T. Ishida, K. Shibamoto, T. Honma, H. Ohashi, T. Murayama and M. Haruta, *ACS Catal.*, 2019, **9**, 8364–8372.
- 22 T. Noor, Y. Qi and D. Chen, *Applied Catalysis B: Environmental*, 2020, **264**, 118430.
- 23 J. Cortés, E. Valencia, J. Herrera and P. Araya, *J. Phys. Chem. C*, 2007, **111**, 7063–7070.